KEK Preprint 91-135
October 1991
H

Energy Dependent Measurements of the *p-p* Elastic Analyzing Power and Narrow Dibaryon Resonances

Y. KOBAYASHI, K. KOBAYASHI, T. NAKAGAWA,

H. SHIMIZU, H.Y. YOSHIDA, H. OHNUMA,

J.A. HOLT, G. GLASS, J.C. HIEBERT, R.A. KENEFICK, S. NATH,

L.C. NORTHCLIFFE, A.J. SIMON,

S. HIRAMATSU, Y. MORI, H. SATO, A. TAKAGI, T. TOYAMA, A. UENO,

and

K. IMAI

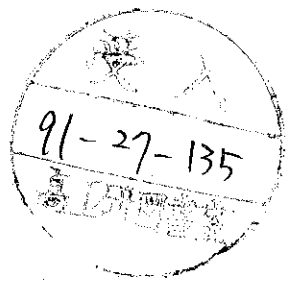

Submitted to Nuclear Physics A.

National Laboratory for High Energy Physics, 1991

KEK Reports are available from:

Technical Information & Library
National Laboratory for High Energy Physics
1-1 Oho, Tsukuba-shi
Ibaraki-ken, 305
JAPAN

Phone: 0298-64-1171
Telex: 3652-534 (Domestic)
(0)3652-534 (International)
Fax: 0298-64-4604
Cable: KEKOHO

ENERGY DEPENDENT MEASUREMENTS OF THE *p-p* ELASTIC ANALYZING POWER AND NARROW DIBARYON RESONANCES

Y. KOBAYASHI[1], K. KOBAYASHI[2], and T. NAKAGAWA

Department of Physics, Tohoku University, Sendai 980, Japan

H. SHIMIZU[3], H.Y. YOSHIDA , and H. OHNUMA

Department of Physics, Tokyo Institute of Technology, Tokyo 152, Japan

J.A. HOLT[4], G. GLASS, J.C. HIEBERT, R.A. KENEFICK, S. NATH[5], L.C. NORTHCLIFFE, and A.J. SIMON

Texas A&M University, College Station, Texas 77843, USA

S. HIRAMATSU, Y. MORI, H. SATO, A. TAKAGI, T. TOYAMA, and A. UENO

National Laboratory for High Energy Physics (KEK), Tsukuba 305, Japan

K. IMAI

Department of Physics, Kyoto University, Kyoto 606, Japan

---

[1] Present address: National Laboratory for High Energy Physics (KEK), Tsukuba 305, Japan.

[2] Present address: NEC Co. Ltd., Kawasaki 213, Japan.

[3] Present address: Department of Physics, Yamagata University, Yamagata 990, Japan.

[4] Present address: Fermi National Accelerator Laboratory, Batavia, Il 60510, USA

[5] Present address: Los Alamos National Laboratory, Los Alamos, NM 87545, USA.

Abstract

The energy dependence of the *p-p* elastic analyzing power has been measured using an internal target during polarized beam acceleration. The data were obtained in incident-energy steps varying from 4 to 17 MeV over an energy range from 0.5 to 2.0 GeV. The statistical uncertainty of the analyzing power is typically less than 0.01. A narrow structure is observed around 2.17 GeV in two proton invariant mass distribution. A possible explanation for the structure with narrow resonances is discussed.

Keyword

NUCLEAR REACTIONS ^{1}H(polarized p, pp), E=0.5-2.0 GeV; measured analyzing power (A(E), θ_{lab}=68.0°), internal polyethylene string target.

1. Introduction

Understanding the nucleon-nucleon (N-N) interaction is one of the most fundamental problems of nuclear physics. Because of the rich complexity brought on by its dependence on the spin S, isospin I, relative momentum p, and orbital angular momentum l of the nucleons, the problem remains incompletely solved despite the intensive experimental and theoretical effort devoted to its investigation over the past forty years or more. In particular, the description of the interaction becomes quite complex as the nucleon laboratory energy E_N is increased. A great deal is known, however, about the N-N interaction in the low energy region where a phase shift analysis is feasible. It is known that the phase shifts (and the coupling parameters) for the partial waves of higher l are well represented by those for one-boson exchange (OBE), and those for lower l can be determined empirically. Such a phase shift set represents a complete experimental solution to the problem, and a common ground for the meeting of experiment and theory. Such sets of phase shifts have been uniquely, if not precisely, determined for laboratory energies E_N up to several hundred MeV, primarily because of the influx of new data from the "meson factories" at LAMPF, TRIUMF, and PSI. As the energy increases, however, the description of the interaction becomes quite complex because pion production starts to happen and then Δ and N^* resonances are encountered, and it becomes necessary to determine an inelasticity parameter for each partial wave, doubling the number of parameters to be determined.

The partial wave representation becomes more and more cumbersome. On the other hand, the experimental data above 1 GeV are quite scarce, especially in the spin observables (analyzing power and spin correlation parameters). Therefore the accumulation of experimental data in the N-N observables is desired in order to extend the description of the N-N interaction to higher energies above 1 GeV.

Anomalies have been found experimentally in the spin dependence of the N-N total cross section between 0.5 and 1.0 GeV [1]) at Argonne National Laboratory (ANL). The explanation of these has led to considerable speculation on the existence of dibaryon resonances, or relatively long-lived six quark exotic states [2]). It is now widely believed that nucleons and mesons are composed of quarks confined somehow in bags, perhaps surrounded by clouds of virtual pions, and that while the long-range part of the N-N interaction is explainable in terms of pion exchange and the shorter range part by additional exchange of other mesons (ρ, ω, σ, etc.), the ultimate explanation of the extremely short-range part explored in hard collisions at high energy will be in terms of quark exchange or quark-quark interactions. Some bag-model calculations predict six-quark states which are relatively narrow in width [3-4]), and thus might be detectable.

Recently, several narrow structures have been observed in the missing mass and the invariant mass spectra of two nucleons in few body nuclear reactions [5-7]). The interpretation of the spectra is, however, not straightforward due to the complexity introduced by

the nucleus. Thus the N-N scattering observables measured in small energy steps (~5MeV) play an important role in the determination of the existence of such narrow structures. At present there are unfortunately few experiments [8-10] with such fine energy dependent measurements in the N-N channel, since it is rather difficult to change the incident beam energy in such small steps.

We measured the energy dependence of the p-p elastic analyzing power using an internal target during beam acceleration. Internal string targets available at many accelerators in the world have mainly been used for tuning to get past depolarizing resonances. This availability enabled us to make measurements in fine energy steps (excitation functions). This technique is, therefore, useful in a search for narrow structures. This is the first experiment using an internal string target in an analyzing power measurement. A brief report of this experiment has already been published [11]. In the present paper we describe the experimental procedure and the analysis in detail.

2. Experimental Method

The experiment was performed at the National Laboratory for High Energy Physics (KEK) using a polarized proton beam. In order to obtain the energy dependence of the p-p elastic analyzing power in fine incident-energy steps over a wide energy range, the measurement was made during acceleration with an internal target system and a detector assembly installed in a straight section of the main ring proton synchrotron (PS).

2.1 POLARIZED PROTON BEAM

Polarized H^- ions are produced in an optically pumped polarized ion source [12]. The H^- beam is accelerated by a 750 keV Cockcroft-Walton pre-injector and a 40 MeV linac, and injected into a booster synchrotron where charge-exchange injection is employed. The polarized proton beam is then accelerated up to 0.5 GeV in the booster. Five bunches of the beam are injected into the main ring synchrotron with the repetition rate of 10 Hz to be accelerated up to the final energy of 3.5 GeV. The number of circulating protons in the main ring was typically 1×10^9 in the present experiment.

Maintenance of the spin alignment of the polarized beam in the KEK PS is a problem, because there are alternating vertical and horizontal focusing fields in this strong focusing type accelerator. The horizontal fields in quadrupole magnets can cause depolarization of the beam. Depolarizing resonance occurs when the frequency components of the horizontal fields seen by the particle are equal to the particle spin precession frequency γG, where γ is the Lorentz energy factor and G is the anomalous gyromagnetic ratio for the proton. A depolarizing resonance takes place at

$$\gamma G = nN \pm \nu_z , \qquad (2.1)$$

where n is an integer, N is the superperiodicity of the machine, and ν_z is the vertical betatron tune (N=4 and ν_z = 6.25 for the KEK PS). Such a depolarizing resonance is called intrinsic. In addition, unavoidable imperfections in the alignment of the magnets of the

accelerator cause displacements in the beam orbit called "closed orbit distortion (COD)." These imperfection resonances can also cause the depolarization of the beam. There is one at

$$\gamma G = nN \pm k, \qquad (2.2)$$

where k is the harmonic number of the COD. Table 1 shows the location of the intrinsic and imperfection resonances from 0.5 to 3.5 GeV in the KEK PS. The beam polarization can not be maintained during acceleration without use of several methods to suppress the depolarizing resonances. A detailed description of the methods employed at the KEK PS has been presented by H. Sato [13]. With these methods the beam polarization was maintained to be about 0.45 at 0.5 GeV and about 0.35 at 3.5 GeV during this experiment. Furthermore, in order to make asymmetry measurements, the spin orientation of the polarized beam was flipped in the ion source every acceleration cycle (duration = 2.5 sec).

2.2 INTERNAL TARGET

The effective beam intensity was very high because of multiple traverses of the beam through the target (about 10^6 times higher than that of the extracted beam). On the other hand, there was a lower limit to the beam intensity dictated by the need to maintain stable acceleration. Therefore a very thin polyethylene string (30 μm in diameter) was used as the internal target. The target system shown in fig.1 consisted of two independent rotating-frames on which the polyethylene string and a similar string of carbon were mounted

respectively. The angle of rotation for each frame was monitored by a variable capacitance sensor attached to the axis of rotation. This system enabled one of the targets to flip into the beam quickly during acceleration and to settle down within 80 msec. The polyethylene string target was flipped to the beam position 100 msec before the start of acceleration. The alternate carbon fiber target was also used in the present experiment to estimate the background events from quasi-free p-p scattering (p-p scattering from a proton bound in one of the target carbon nuclei).

2.3 DETECTOR SYSTEM

The detector system was a polarimeter, which consisted of a left-right symmetric four arm system to detect the left (right) forward-scattered proton in coincidence with the conjugate right (left) backward-recoil proton. A schematic view is shown in fig.2. In the backward arm a small scintillator telescope, B_1 and B_2, was employed. The scattering angle and the angular acceptance for p-p elastic scattering were defined by the telescope. The angle of the backward telescopes was set to be 68.0° since the analyzing power for p-p elastic scattering was known to be almost maximum at this angle in the energy region from 0.5 to 2.5 GeV. The uncertainty of the angle was about ± 0.1° and the angular acceptance was ± 0.7°. Each forward scintillation-counter assembly was composed of six adjacent vertical bars $X_1,\ldots,X_6$ in tandem with five adjacent horizontal bars $Y_1,\ldots,Y_5$. Thus the forward detector assembly had thirty cells defined by the coincidences $X_i \cdot Y_j$ and served as a position sensitive

detector. The forward detectors were placed so that true coincidence events of p-p elastic scattering were concentrated on the (X_i,Y_3) cells. This set-up covered a wide energy range of about 2.0 GeV. A pair of monitor scintillation counters were set at 75.0° to monitor the beam condition (polarization, intensity, etc.) during acceleration throughout the experiment. The sizes of these detector elements and their distances from the target are given in table 2.

2.4 BEAM POLARIZATION MONITOR

In addition to the polarimeter mentioned above, a similar polarimeter (called the injection polarimeter) was also installed at a straight section in the main ring and used to measure the polarization of the beam at 0.5 GeV before the start of acceleration. The forward and backward angles of the detectors here were fixed at 21.2° and 63.9°, respectively. Event triggers were formed by the coincidence of two forward scintillation-counters and the conjugate backward detector and sent to a CAMAC scaler. The first of five injected bunches was used to strike a polyethylene string target (about 150 μm in diameter) at the injection polarimeter. Subsequently this target was removed from the beam position before the next bunch was injected. The data from the injection polarimeter was monitored by an on-line computer during the experiment.

2.5 DATA ACQUISITION

A schematic diagram of acceleration cycle along with the timing for data-taking is shown in fig.3. This figure shows one cycle of polarized

beam acceleration. The injection of polarized protons from the booster to the main ring starts at P1. The beam begins accelerating at P2 and reaches its peak energy, the flat-top, at P3.

Data-taking started at P2 and continued for 220 msec. The data were acquired with a DEC μVAX computer connected to a CAMAC hardware system via a Kinetic Systems k3922 crate controller. The k3922 controlled several 8k byte buffer memories which were placed in the master crate. The acquisition electronics modules were placed in each slave crate connected to the buffer memory via a 16-bit data bus. At a time, 400 msec after P3, all of the data accumulated in the buffer memories were sent to the computer and written on magnetic tapes.

In this experiment CAMAC 100 MHz scalers were used to accumulate forward-backward coincidence events since the fast acquisition time was required to handle a high instantaneous counting rate. The left (right) event for the scalers was defined by $LX_i \cdot LY_j \cdot RB_1 \cdot RB_2$ ($RX_i \cdot RY_j \cdot LB_1 \cdot LB_2$). The coincidence width 2τ was set to be 20 nsec. Two groups of scalers (CH1 and CH2) counting the same coincidence combinations were used in order to realize a continuous measurement with a short interval of 1 msec. They were activated to receive signals in alternate intervals. These signals were passed through a router. While one group of scalers (CH1) were on data-taking status, the others (CH2) were inhibited and the data taken in the previous 1 msec interval were sent to a buffer memory.

In addition to the scaler data the time differences between several forward and backward detectors were measured with a

sampling method which made use of CAMAC time to digital converters (TDCs) to estimate the accidental coincidence rates. A 1 kHz clock was used to tag the TDC events so that the beam energy for the event could be determined. This depended on knowledge of the accelerator magnetic field pattern as a function of time measured from P2. From this pattern the relative kinetic energy of the beam could be determined.

The spin state of the beam was indicated by two signals from the ion source. When one was true the other was false. For an unpolarized beam they were both false. These two signals were read into a CAMAC coincidence register at the start of each acceleration cycle.

3. Data Reduction

The data analysis was made using an off-line computer in the KEK Computer Center.

3.1 SELECTION OF *p-p* ELASTIC EVENTS

Three dimensional histograms of coincidence events detected in the forward detector cells and the backward telescope are shown in fig.4. These are typical examples of data in all energy bins. The *p-p* elastic events form sharp peaks in the histograms due to the kinematical angular correlation and the coplanarity condition. As the incident energy increases, the peak position moves from X_6 to X_1 due to the kinematics, while it always centers on Y_3 because of coplanarity. Thus *p-p* elastic events can be roughly identified.

However, the broad background events are distributed over the detection cells. In addition to the background events, accidental coincidence events contained in the histograms have to be subtracted. Therefore in order to get true *p-p* elastic events from the peak it is necessary to evaluate the background events and accidental coincidence events and subtract them.

First the accidental coincidence rate in the scaler data is evaluated using the TDC data. A typical TDC spectrum is shown in fig.5. The lower part is the same spectrum as the upper part except that the vertical scale is increased to show the distribution of the accidental coincidence events. The FWHM of the peak is about 1.2 nsec which indicates the time resolution for the TDC measurement. The shaded area, within 20 nsec, shown in the lower part corresponds to the accidental coincidence events in the scaler data. The solid line shows the result of fitting the accidental event distribution with a polynomial function. The accidental coincidence rate is evaluated from the ratio of the events within 20 nsec centering on the peak to the events distributed on the foot of the peak. As a result the rate is 1.6 % around 0.5 GeV and gradually increases to 6.7 % around 2.0 GeV.

After correction for the accidental coincidence events, background events due to quasi-free *p-p* scattering and many body reactions are subtracted using information provided with the (X_i, Y_1) and (X_i, Y_5) cells together with the data taken with the carbon target. As an example, fig.6 shows coincidence events detected on the (X_4, Y_3) cell as

a function of incident beam energy. The background rate for overall events is 1.9 % around 0.5 GeV and 7.1 % around 2.0 GeV.

3.2. RAW ASYMMETRY

The p-p elastic events after subtraction of the accidental and the background events are sorted by left or right scattering and the beam spin states. Figure 7 shows the sorted events versus incident beam energy from 0.5 to 2.0 GeV. Total integrated counts in each energy bin are represented by the following equations,

$$\begin{aligned} N_L^{\uparrow} &= n_T I_B^{\uparrow} \sigma(\theta_L) \Delta\Omega_L \left\{1 + p_B^{\uparrow} \cdot A_y(\theta_L)\right\} , \\ N_L^{\downarrow} &= n_T I_B^{\downarrow} \sigma(\theta_L) \Delta\Omega_L \left\{1 - p_B^{\downarrow} \cdot A_y(\theta_L)\right\} , \\ N_R^{\uparrow} &= n_T I_B^{\uparrow} \sigma(\theta_R) \Delta\Omega_R \left\{1 - p_B^{\uparrow} \cdot A_y(\theta_R)\right\} , \\ N_R^{\downarrow} &= n_T I_B^{\downarrow} \sigma(\theta_R) \Delta\Omega_R \left\{1 + p_B^{\downarrow} \cdot A_y(\theta_R)\right\} , \end{aligned} \qquad (3.1)$$

where the superscripts $\uparrow(\downarrow)$ and subscripts $L(R)$ denote the beam spin-up (down) state and scattering directions, left (right). The n_T and I_B are the number of protons in the target and the beam, respectively, $\sigma(\theta)$ is the differential cross section, $\Delta\Omega$ is the solid angle of the detection system, and p_B and $A_y(\theta)$ are beam polarization and the analyzing power, respectively. We define the raw asymmetry ε as

$$\varepsilon = \frac{r-1}{r+1}, \qquad (3.2)$$

where r is the ratio

$$r = \sqrt{\frac{N_L^{\uparrow} N_R^{\downarrow}}{N_L^{\downarrow} N_R^{\uparrow}}} . \qquad (3.3)$$

It can be rewritten by

$$\varepsilon = \bar{p} \cdot \bar{A} \left\{1 + \frac{(\Delta p \cdot \bar{A})^2 + (\bar{p} \cdot \Delta A)^2 - 2\Delta p \cdot \Delta A}{2(1 - \bar{p}^2 \cdot \bar{A}^2)}\right\} . \qquad (3.4)$$

Here $\bar{p}$, Δp, and $\bar{A}$ and ΔA are represented as follows:

$$\bar{p} = \frac{p_B^{\uparrow} + p_B^{\downarrow}}{2} , \quad \Delta p = \frac{p_B^{\uparrow} - p_B^{\downarrow}}{2} ,$$

$$\bar{A} = \frac{A_y(\theta_L) + A_y(\theta_R)}{2} , \quad \Delta A = \frac{A_y(\theta_L) - A_y(\theta_R)}{2} . \qquad (3.5)$$

Other quantities n_T, I_B , $\sigma(\theta)$, and $\Delta\Omega$ shown in eq.(3.1) cancel in formula r. Furthermore when the differences of the beam polarizations, Δp, and the analyzing powers, ΔA, are small, the second order difference terms are negligible. Actually the Δp turned out to be small enough (Δp=0.017). The ΔA is also small (ΔA<<0.01) since the analyzing power is known to be almost maximum and flat in the vicinity of our set-up angle. Therefore the raw asymmetry can be expressed by a very simple formula,

$$\varepsilon = \bar{p} \cdot \bar{A} . \qquad (3.6)$$

This is just a product of the average beam polarization and the average analyzing power. We obtained simultaneously three different asymmetries shown in fig.8(a)-(c). Figure (a) is the raw asymmetry for p-p elastic scattering, and others are those for inclusive reactions detected by backward telescopes and by monitor

counters. These asymmetries give an important information on the beam polarization during acceleration. We will discuss the asymmetries later.

3.3 BEAM POLARIZATION

The average beam polarization $\bar{p}$ was measured at 0.5 GeV to be 0.46 using the injection polarimeter. We assume, at first, constant beam polarization over the energy region of this experiment. This assumption might be acceptable if there are no depolarizing resonances during polarized beam acceleration. However there exist three imperfection resonances capable of causing depolarization of the beam at $\gamma G=3$, 4, and 5 in this energy region. The corresponding beam energies are indicated with vertical dash-dotted lines in fig.8. As far as these imperfection resonances are concerned, fortunately, their strengths are estimated to be very weak and their widths are calculated to be much less than one energy bin [13]). Thus, the beam polarization and consequently the measured asymmetry are expected to decrease like a small step function at the energy bin where depolarization occurs. No such step is seen in fig.8(a) at the beam energy corresponding to $\gamma G=3$ and 5, but a small step is apparent at 1.155 GeV corresponding to $\gamma G=4$. Similar behavior is seen in the data taken with backward telescopes and with monitor counters as shown in fig.8(b),(c). Consequently the beam polarization was determined to be 0.46 for incident beam energy up to 1.155 GeV and 0.44 for the remaining range of beam energy covered by the present data.

3.4 INCIDENT BEAM ENERGY

The incident beam energy is derived as follows. In a synchrotron the magnetic rigidity is variable during acceleration and its value is accurately known. The momentum p of the beam circulating in the synchrotron ring is proportional to the magnetic rigidity $B\rho$. We have

$$p_i=\alpha(B\rho)_i\,, \tag{3.7}$$

where α is a constant and subscript i denotes the time from P2. The absolute momentum can be precisely determined if the momentum p_o at a reference time, $i=0$, is well known. It is given by

$$p_i=\frac{(B\rho)_i}{(B\rho)_0}p_0\,. \tag{3.8}$$

Two different timings at which strong depolarizing resonances, $\gamma G=\nu_z$ and $\gamma G=7$, take place are used as the reference timing where the sign of the beam polarization flips in crossing these resonances [13]). The beam momenta corresponding to the depolarizing resonances are obtained by

$$p=m_p\sqrt{\gamma^2-1}\quad\left(\gamma=\frac{7}{G}\ or\ \frac{\nu_z}{G}\right), \tag{3.9}$$

where m_p is the rest mass of the proton. As shown in fig.9, the timing of the spin flip on the resonances can be found by the point where the sign of the raw asymmetry for p-p scattering reverses.

The position of the spin flip is determined within 1.0 msec accuracy. This corresponds to about 0.5%, in incident beam momentum, which is almost equal to the momentum spread in the KEK PS.

4. Experimental results

The analyzing power $\bar{A}$ for p-p elastic scattering is simply calculated from the raw asymmetry ε divided by beam polarization $\bar{p}$. The statistical uncertainty $\Delta\bar{A}$ is given by

$$\Delta\bar{A}=\frac{1}{\bar{p}}\sqrt{\Delta\varepsilon^2+(\varepsilon\frac{\Delta\bar{p}}{\bar{p}})^2}, \qquad (4.1)$$

where

$$\Delta\varepsilon=\frac{(1-\varepsilon^2)}{4}\sqrt{\frac{1}{N_L^{\uparrow}}+\frac{1}{N_L^{\downarrow}}+\frac{1}{N_R^{\uparrow}}+\frac{1}{N_R^{\downarrow}}}. \qquad (4.2)$$

The numerical results are given in table 3. The scattering angle in the center of mass system, $\theta_{C.M.}$, decreases gradually with increasing incident beam energy because the measurement was made at the fixed backward laboratory angle. Figure 10 shows the p-p elastic analyzing power as a function of incident energy. The present results are in good agreement with phase-shift predictions SM88 [14] in which the present data are not taken into account. The statistical uncertainty of the analyzing power is typically less than 0.01. The systematic uncertainty is estimated to be about ±0.025 for the data up to 1.155 GeV and ±0.035 for the remaining data. This comes

primarily from the uncertainty in the absolute value of beam polarization.

Two prominent narrow peaks are observed at incident energies of 0.61 and 0.68 GeV, which correspond to p-p invariant mass values 2.16 and 2.19 GeV, respectively [11].

5. Discussion

5.1 NARROW STRUCTURE

Here is still a serious question on the experimental result as follows: If there is a complicated polarization distribution across the beam spot, does it give rise to the observed structure (two narrow peaks) since the beam moves over the internal string target during acceleration? Furthermore, the observed structure is located near and might be caused by the depolarizing resonance with $\gamma G=3$. To address these questions we have measured the asymmetry for the inclusive reactions at the same time and with the same set-up but with logic different from that for p-p elastic scattering. We directly measure asymmetries instead of analyzing powers and assume constant beam polarization to get the analyzing powers. Therefore if the beam polarization changes during acceleration and consequently it makes an illusive structure in the elastic analyzing power a similar effect should also be observed in the asymmetry for the inclusive reactions measured simultaneously. Figure 8(b) shows the energy dependence of the asymmetry in the inclusive reactions such as $pp\rightarrow pX$, $pp\rightarrow\pi X$, $pC\rightarrow pX$, $pC\rightarrow\pi X$, and so forth, at the laboratory

backward angle of 68°. No structure is seen near $\gamma G=3$ as shown in fig.8(b) nor in fig.8(c) which displays the energy dependence of the asymmetry in the inclusive reactions measured with the monitor counters. Thus the structure observed around 0.65 GeV in the elastic analyzing power is considered to be real.

5.2 NARROW RESONANCE

We have attempted to reproduce the structure observed in the p-p elastic analyzing power by introducing a narrow resonance in a partial wave, one by one. In order to describe the smooth background we employ the energy dependent amplitudes deduced from Arndt's global phase shift analysis SM88 based on the energy independent analyses which have been made in about 50 MeV steps in the relevant energy region. There is no room for narrow resonances in the solution SM88 due to the coarse steps. Thus we can add narrow resonance terms to the Arndt's energy dependent amplitudes. An elastic S-matrix element can then be written as

$$S_{el} = \eta_B e^{2i\delta_B+2i\delta_R+i\phi}, \qquad (5.1)$$

where δ_B and η_B are Arndt's real phase shift and reflection parameter for a partial wave, respectively, δ_R is a complex resonance phase, and ϕ is a relative phase between the background amplitudes and the resonance amplitude. Assuming a Breit-Wigner type resonance in eq. (5.1) we get a T matrix element

$$T_{el} = \frac{-\Gamma_{el}}{2(E-E_R)+i\Gamma}\eta_B e^{2i\delta_B+i\phi} + \frac{\eta_B e^{2i\delta_B+i\phi}-1}{2i}. \qquad (5.2)$$

Here E denotes the total energy, E_R corresponds to a resonance energy, and Γ and Γ_{el} are the total width and the elastic width, respectively. The elasticity η of the resonance is defined by

$$\eta=\Gamma_{el}/\Gamma. \qquad (5.3)$$

The relative phase ϕ is chosen to be 0 to maintain the unitarity condition of the T matrix. At this level of discussion, the previously existing data are still sparse except for the energy dependent differential cross section data, at $\theta_{C.M.}=90°$, taken at LNS [9] and the energy dependent n-p total cross section data obtained at LAMPF [8]. Both of them show no narrow structure and are already taken into account in the SM88 analysis. Therefore we cannot improve the situation in reproducing the differential cross section and the total cross section by adding narrow resonance terms to the SM88 amplitudes. The question is whether we can reproduce the structure observed in the analyzing power by introducing the resonance terms without having any big influence on the energy dependence of the differential cross section and the total cross section.

Figures 11-14 show the analyzing power, the differential cross section, and the total cross section for p-p scattering as a function of the two-proton invariant mass. The analyzing power data in these figures are essentially the same as those shown in the lower energy

region of fig.10. At first we investigate the effects of a narrow resonance in the ^3P waves with the resonance parameters, $E_R=2.170$ GeV, $\Gamma=15$ MeV and $\eta=0.1$. The results are shown in fig.11, where the solid curves correspond to predictions of SM88 + the resonance in each of the ^3P waves and the dash-dotted lines represent predictions of SM88 only. Figure 11(a) shows the results when we include the narrow resonance in the $^3P_0$ partial wave. This can not reproduce the analyzing power data. When the narrow resonance is introduced in the $^3P_1$ wave there is acceptable reproduction of the first peak around 2.16 GeV as shown in the upper part of fig.11(b). This resonance, however, produces an undesirable effect on the elastic differential cross section (the middle part of fig.11(b)). It is possible for a resonance in the $^3P_2$ wave to reproduce the structure and to give no large effects on the cross sections if the elasticity η of this resonance is chosen to be about 0.04. The p-p total cross section data, unfortunately, can not bear the relevant discussion on the narrow resonance because of many different normalizations. As for the n-p total cross section there exist fine-energy dependent data which are displayed in the lower part of fig.11, together with the p-p total cross section data [16]. We also calculate the n-p total cross section with the narrow resonance and display results with dashed lines in the figure.

Figure 12 shows the results when a narrow resonance is inserted in the ^3F waves one by one with the same resonance parameters as before. The narrow resonance in the $^3F_3$ reproduces the structure in the analyzing power without producing a large effect on the differential cross section with the elasticity of η=0.1, while it gives

the same effect on the p-p or n-p total cross section as the resonance in the $^3P_2$ wave does. A $^3F_4$ resonance gives a clear bump around the resonance energy in the differential cross section.

The calculated results when a narrow resonance is added into each of the ^3H waves are displayed in fig.13. Compared with the case of lower partial waves, the effects of the resonance on the observables become larger due to an enhancement factor of higher partial wave in the amplitudes. Both of the resonances in the $^3H_4$ and $^3H_6$ waves make large dips in the analyzing power. There is a possibility that a $^3H_5$ resonance can reproduce the structure with a small elasticity of $\eta\approx0.03$.

Although the singlet partial waves do not contribute to the product of analyzing power and differential cross section, they may give some contribution to the analyzing power. Figure 14 displays the results in the case of the singlet partial waves, $^1S_0$, $^1D_2$ and $^1G_4$ with the same resonance parameters as before. A $^1S_0$ resonance can account for the structure in the analyzing power with producing a small effect on the differential cross section if $\eta\approx0.2$ is employed (η=0.1 in fig.14). By contrast the resonance in the $^1G_4$ wave can reproduce the structure with a smaller elasticity $\eta\approx0.05$ although a sizable effect of the resonance still remains in the differential cross section and the total cross section.

In the present analysis we find that the elasticity of a narrow resonance must be very small whenever the resonance reproduces the structure in the analyzing power well. This could account for the

fact that narrow structures have not been observed previously in the N-N channel.

6. Summary

The continuous energy dependence of the p-p elastic analyzing power has been measured during polarized beam acceleration using an internal target. This experiment is the first demonstration as physics run performed inside the tunnel of the KEK PS. We have obtained systematic data in fine incident-energy steps. The statistical uncertainty of the analyzing power is typically less than 0.01. A narrow structure is observed around 2.17 GeV in the two proton invariant mass distribution of the analyzing power. We have tried to explain the structure by introducing a narrow resonance. A resonance in any of the ${}^3P_2$,${}^3F_3$ and ${}^3H_5$ waves can reproduce the structure in the analyzing power without producing a large effect on the differential cross section or the total cross section, as shown in fig.15. The resonance parameters are chosen as follows: $E_R=2.170$ GeV, $\Gamma=15$ MeV and $\eta=0.04$ for the ${}^3P_2$ wave; $E_R=2.165$ GeV, $\Gamma=15$ MeV and $\eta=0.1$ for the ${}^3F_3$ wave; $E_R=2.160$ GeV, $\Gamma=15$ MeV and $\eta=0.03$ for the ${}^3H_5$ wave. There is another possibility that a resonance in the ${}^1S_0$ wave accounts for the structure. We find the elasticity of any of these resonances very small. It is expected to accumulate fine-energy dependent data for other observables in the N-N channel to solve the relevant problem about such a narrow resonance.

We would like to thank the KEK PS operating crew for stable operation of the polarized beam during the experiment and express our gratitude to the accelerator division staff for their efficient help in preparations for the experiment. We also wish to thank Professor K. Nakai and Professor K. Takamatsu for their encouragement and assistance throughout this work. One of the authors (Y. K) is indebted to Professor T. Tohei for his kindly guidance and encouragement. This experiment was supported in part by the U.S. Department of Energy under Grant No. DE-FG05-88ER40399.

References

1) I.P. Auer *et al.*, Phys. Lett. **67B** (1977) 113; **70B** (1977) 475; Phys. Rev. Lett. **41** (1978) 354

2) See, for example, M.P. Locher, M.E. Sainio, and A. Svarc, Adv. Nucl. Phys. **17** (1986) 47; M.M. Makarov, Sov. J. Part. Nucl. **15** (1984) 419

3) P.La France and E.L. Lomon, Phys. Rev. **D34** (1986) 1341; P. González, P.La France, and E.L. Lomon, Phys. Rev. **D35** (1987) 2142

4) S.M. Dorkin, V.K. Lukyanov, and A.I. Titov, Z. Phys. **A316** (1984) 331

5) B. Tatischeff, P. Berthet, M.P. Combes-Comets, J.P. Didelez, R.Frascaria, Y.Le Bornec, A. Boudard, J.M. Durand, M.Garçon, J.C. Lugol, Y. Terrien, R.Beurtey, and L. Farvacque, Phys. Rev. **C36** (1987) 1995; Phys. Rev. Lett. **52** (1984) 2022

6) B. Bock, W. Ruhm, K.H. Althoff, G. Anton, W. Ferber, H.W. Gelhausen, T. Jahnen, O. Kaul, D. Menze, W. Meyer, T. Miczaika, E.

Roderburg, E. Schilling, E. Schenuit, D. Sundermann, and W.J. Schwille, Nucl. Phys. **A459** (1986) 573

7) L. Santi, M. Barlett, D. Ciskowski, R. Garfagnini, M.M. Gazzaly, G.W. Hoffmann, K.W. Jones, M.A.Nasser, G. Pauletta, C. Smith, N.Tanaka, and R. Whitney, Phys. Rev. **C38** (1988) 2466

8) P.W. Lisowski, R.E. Shamu, G.F. Auchampaugh, N.S.P. King, M.S. Moore, G.L. Morgan, and T.S.Singleton, Phys. Rev. Lett. **49** (1982) 255

9) M. Garçon, D. Legrand, R.M. Lombard, B. Mayer, M. Rouger, Y. Terrien, and A. Nakach, Nucl. Phys. **A445** (1985) 669

10) M. Garçon, J.C. Duchazeaubeinex, J.C. Faivre, B. Guillerminet, D. Legrand, M.Rouger, J. Saudinos and J. Arvieux, Phys. Lett. **B183** (1987) 273

11) H. Shimizu, H.Y. Yoshida, H. Ohnuma, Y. Kobayashi, K. Kobayashi, T. Nakagawa, J.A. Holt, G. Glass, J.C. Hiebert, R.A. Kenefick, S. Nath, L.C. Northcliffe, A. Simon, S. Hiramatsu, Y. Mori, H. Sato, A. Takagi, T. Toyama, A. Ueno, and K. Imai, Phys. Rev. **C42** (1990) R483

12) Y. Mori, T. Ikegami, A. Takagi, and S. Fukumoto, 4th Int. Symp. on Production and Neutralization of Negative Ions and Beams, Brookhaven, 1986, AIP Conf. Proc. No.158 (1986) p.605; Proc. 6th Symp. on Acc. Sci. and Tech. (1987) p.68

13) H. Sato, Jpn. J. Appl. Phys. **27** (1988) 1022; H. Sato *et al.*, Nucl. Inst. and Meth. **A272** (1988) 617

14) R.A. Arndt, J.S. Hyslop III, and L.D. Roper, Phys. Rev. **D35** (1987) 128; the computer code SAID (unpublished), private communication.

15) P. Chatelain *et al.*, J. Phys. **G8** (1982) 643; D. Ottewell *et al.*, Nucl. Phys. **A412** (1984) 189; M.G. Albrow *et al.*, Nucl. Phys. **B23** (1970) 445

16) F. Shimizu *et al.*, Nucl. Phys. **A386** (1982) 571; G.N. Velchko *et al.*, Sov. J. Nucl. Phys. **35** (1982) 852; P. Schwaller *et al.*, Nucl. Phys. **A316** (1979) 317

17) V. Grundies *et al.*, Phys. Lett. **B158** (1985) 15; T.J. Delvin *et al.*, Phys. Rev. **D8** (1973) 136

Table Captions

Table 1. The position of two types of depolarizing resonances of the beam from 0.5 to 3.5 GeV in the KEK PS: (a) intrinsic resonances, (b) imperfection resonances.

Table 2. The size of the detector elements and their distance from the target.

Table 3. Numerical results for p-p elastic scattering as a function of incident beam energy together with two proton invariant mass and the C.M. scattering angle. Quoted uncertainties are purely statistical. The dotted line shows a boundary where beam polarization changes.

Figure Captions

Fig. 1. The internal target system consisting of two independent rotating frames where two string targets are mounted. One is a polyethylene string and the other is a carbon fiber. Each string target measures about 30 μm in diameter.

Fig. 2. Experimental set-up. The symbols of θ_f and θ_b denote the forward and the backward angles of scattered particles, respectively. The scattering angle during acceleration is defined by the backward telescope, B1·B2, set at $\theta_b = 68°$. The size of detection cells in the forward detectors, LFH and RFH, is 25mm×25mm. Monitor counters, LBM and RBM, are set at 75°.

Fig. 3. Schematic diagram of acceleration and data-taking timing.

Fig.4. Three dimensional histograms of the events detected on the forward detector cells in coincidence with signals from the backward telescope. The quoted time measures from acceleration start timing P2. There is a one-to-one correspondence between the time from P2 and the incident beam energy E_p as described in section 3.4.

Fig. 5. A typical TDC spectrum of the time difference between the forward and backward detectors. The shaded area shows the accidental coincidence events. The width of 20 nsec corresponds to

the coincidence width 2τ between the forward detection cells and the backward telescope in the scaler measurement.

Fig. 6. Time (incident energy) dependence of coincidence events detected on the (X_4, Y_3) cell. The dotted line shows accidental coincidence events. The crosses display a sum of the accidental events and the background events.

Fig. 7. Total events for *p-p* elastic scattering as a function of the incident beam energy after subtraction of the accidental and background events. Open circles and squares denote left-up and left-down events, respectively. Vertical and diagonal crosses denote the right-up and right-down events, respectively.

Fig. 8. Raw asymmetries as a function of the incident beam energy: (a) for *p-p* elastic scattering events, (b) for inclusive reactions detected by the backward telescopes and (c) for inclusive reactions detected by the monitor counters. The dot-dashed lines indicate the positions of depolarizing resonances, γG=3, 4, and 5.

Fig. 9. A plot of the raw asymmetry as a function of time from P2. The locations of the depolarizing resonances of $\gamma G = \nu_z$ and 7 are marked with arrows. The data were taken with the monitor counters.

Fig. 10. The energy dependence of the *p-p* elastic analyzing power measured at the laboratory backward angle of 68°. Correction for the

beam polarization is made for the apparent depolarization of the beam at γG=4. The solid curve in the insert shows the Arndt phase-shift prediction (SM88) in which the present data are not taken into account.

Fig. 11 The calculated results with a narrow resonance in each of the ^3P waves in comparison with the experimental observables for *p-p* and *n-p* scattering: in the case of (a) the $^3P_0$ wave, (b) the $^3P_1$ wave, and (c) the $^3P_2$ wave. The resonance parameters are E_R=2.170 GeV, Γ=15 MeV and η=0.1. The solid curves correspond to predictions of SM88 + the resonance in each wave and the dash-dotted lines present predictions of SM88 only. Experimental data in the upper part are the *p-p* elastic analyzing power measured in this experiment. The *p-p* elastic differential cross section data near $\theta_{C.M.}$=90° [9,15]) are displayed in the middle part. The *p-p* total cross section data [16]) are shown in the lower part together with the *n-p* total cross section data [8,17]). The closed and open circles correspond to *p-p* and *n-p* scattering, respectively.

Fig. 12. Same as fig.11 but the results when a narrow resonance is input into each of ^3F waves: in the case of (a) the $^3F_2$ wave, (b) the $^3F_3$ wave, and (c) the $^3F_4$ wave.

Fig. 13. Same as fig.11 but the results when a narrow resonance is input into each of ^3H waves: in the case of (a) the $^3H_4$ wave, (b) the $^3H_5$ wave, and (c) the $^3H_6$ wave.

Fig. 14. Same as fig.11 but the results when a narrow resonance is input into each of the singlet waves: in the case of (a) the $^1S_0$ wave, (b) the $^1D_2$ wave, and (c) the $^1G_4$ wave.

Fig. 15. Same as fig.11 but the results with the resonance parameters, (a) E_R=2.170 GeV, Γ=15 MeV and η=0.04 for the $^3P_2$ wave; (b) E_R=2.165 GeV, Γ=15 MeV and η=0.1 for the $^3F_3$ wave; and (c) E_R=2.160 GeV, Γ=15 MeV and η=0.03 for the $^3H_5$ wave.

Table 1

(a)

γG	E_p (GeV)
12-ν_z	2.071
ν_z	2.333

(b)

γG	E_p (GeV)
3	0.632
4	1.155
5	1.679
6	2.202
7	2.725
8	3.249

Table 2

	Height (mm)	Width (mm)	Thickness (mm)	Distance (mm)
B_1	30	10	3	400
B_2	30	18	5	460
$X_{1\text{-}6}$	125	25	5	900
$Y_{1\text{-}5}$	25	150	5	905
BM	30	18	5	800

Table 3

E_p (GeV)	M_{pp} (GeV)	$\theta_{C.M.}$ (deg)	$\bar{A}$	±	$\Delta\bar{A}$
0.491	2.108	39.57	0.510		0.004
0.495	2.110	39.54	0.505		0.006
0.499	2.112	39.50	0.498		0.006
0.504	2.113	39.47	0.493		0.008
0.508	2.115	39.44	0.513		0.008
0.513	2.117	39.40	0.504		0.008
0.518	2.120	39.36	0.519		0.008
0.524	2.122	39.32	0.507		0.007
0.530	2.125	39.27	0.514		0.007
0.537	2.128	39.22	0.533		0.007
0.542	2.131	39.18	0.532		0.010
0.546	2.132	39.15	0.532		0.010
0.550	2.134	39.12	0.529		0.010
0.555	2.136	39.09	0.531		0.010
0.559	2.138	39.05	0.548		0.010
0.563	2.140	39.02	0.545		0.010
0.568	2.142	38.99	0.539		0.010
0.573	2.144	38.95	0.537		0.009
0.578	2.146	38.92	0.539		0.009
0.583	2.148	38.88	0.547		0.009
0.588	2.150	38.84	0.546		0.009
0.593	2.153	38.80	0.547		0.009
0.599	2.155	38.76	0.562		0.009
0.604	2.158	38.72	0.576		0.009
0.610	2.160	38.68	0.573		0.009
0.616	2.163	38.64	0.553		0.009
0.622	2.165	38.59	0.566		0.009
0.628	2.168	38.55	0.552		0.009
0.635	2.171	38.50	0.546		0.009
0.641	2.174	38.46	0.545		0.009
0.648	2.177	38.41	0.541		0.009
0.655	2.180	38.36	0.537		0.009
0.662	2.183	38.31	0.541		0.009
0.669	2.186	38.26	0.547		0.009
0.677	2.189	38.21	0.545		0.009
0.684	2.192	38.16	0.554		0.009

Table 3 (continued)

E_p (GeV)	M_{pp} (GeV)	$\theta_{C.M.}$ (deg)	$\bar{A}$	±	$\Delta\bar{A}$
0.692	2.195	38.10	0.542		0.009
0.700	2.199	38.05	0.543		0.009
0.708	2.202	37.99	0.519		0.009
0.716	2.206	37.94	0.512		0.009
0.724	2.209	37.88	0.501		0.009
0.733	2.213	37.83	0.504		0.009
0.742	2.217	37.77	0.510		0.009
0.750	2.220	37.71	0.492		0.009
0.759	2.224	37.65	0.500		0.009
0.769	2.228	37.59	0.494		0.009
0.778	2.232	37.53	0.494		0.009
0.787	2.236	37.46	0.491		0.009
0.797	2.240	37.40	0.466		0.009
0.807	2.244	37.34	0.467		0.009
0.817	2.248	37.27	0.468		0.009
0.827	2.253	37.21	0.477		0.009
0.838	2.257	37.14	0.464		0.009
0.848	2.261	37.07	0.471		0.009
0.859	2.266	37.00	0.459		0.009
0.870	2.270	36.94	0.456		0.009
0.881	2.275	36.87	0.444		0.009
0.892	2.279	36.80	0.447		0.009
0.904	2.284	36.73	0.432		0.009
0.915	2.289	36.65	0.439		0.009
0.927	2.294	36.58	0.450		0.009
0.939	2.299	36.51	0.438		0.009
0.951	2.303	36.44	0.427		0.009
0.963	2.309	36.36	0.442		0.009
0.976	2.314	36.29	0.424		0.009
0.989	2.319	36.21	0.433		0.009
1.001	2.324	36.14	0.416		0.009
1.014	2.329	36.06	0.422		0.009
1.028	2.335	35.98	0.410		0.009
1.041	2.340	35.91	0.414		0.009
1.055	2.345	35.83	0.395		0.009
1.068	2.351	35.75	0.413		0.009

Table 3 (continued)

E_p (GeV)	M_{pp} (GeV)	$\theta_{C.M.}$ (deg)	$\bar{A}$	±	$\Delta\bar{A}$
1.082	2.356	35.67	0.423		0.009
1.096	2.362	35.59	0.402		0.009
1.111	2.368	35.51	0.415		0.009
1.125	2.373	35.43	0.401		0.009
1.140	2.379	35.35	0.400		0.009
1.155	2.385	35.27	0.389		0.010
1.170	2.391	35.19	0.375		0.010
1.185	2.397	35.11	0.388		0.010
1.200	2.403	35.02	0.395		0.010
1.216	2.409	34.94	0.376		0.010
1.232	2.415	34.86	0.394		0.010
1.248	2.421	34.77	0.394		0.010
1.264	2.427	34.69	0.380		0.010
1.280	2.434	34.61	0.378		0.010
1.296	2.440	34.53	0.388		0.010
1.311	2.446	34.44	0.377		0.010
1.328	2.452	34.36	0.365		0.010
1.344	2.458	34.28	0.386		0.010
1.360	2.464	34.20	0.372		0.010
1.376	2.470	34.12	0.378		0.010
1.392	2.477	34.04	0.370		0.010
1.408	2.483	33.96	0.356		0.010
1.424	2.489	33.89	0.368		0.011
1.440	2.495	33.81	0.367		0.011
1.456	2.501	33.73	0.371		0.011
1.473	2.507	33.65	0.364		0.011
1.489	2.513	33.58	0.339		0.011
1.505	2.519	33.50	0.347		0.011
1.521	2.525	33.42	0.338		0.011
1.538	2.531	33.35	0.367		0.011
1.554	2.537	33.27	0.348		0.011
1.570	2.543	33.20	0.343		0.011
1.587	2.549	33.13	0.342		0.011
1.603	2.555	33.05	0.352		0.011
1.619	2.561	32.98	0.340		0.011
1.636	2.567	32.91	0.323		0.011

Table 3 (continued)

E_p (GeV)	M_{pp} (GeV)	$\theta_{C.M.}$ (deg)	$\bar{A}$	±	$\Delta\bar{A}$
1.652	2.573	32.83	0.332		0.011
1.669	2.579	32.76	0.321		0.011
1.685	2.585	32.69	0.335		0.011
1.701	2.591	32.62	0.314		0.011
1.718	2.597	32.55	0.320		0.011
1.734	2.603	32.48	0.316		0.012
1.751	2.609	32.41	0.330		0.012
1.767	2.615	32.34	0.297		0.012
1.784	2.621	32.27	0.306		0.012
1.800	2.627	32.20	0.314		0.012
1.817	2.633	32.13	0.292		0.012
1.834	2.639	32.06	0.300		0.012
1.850	2.644	32.00	0.314		0.012
1.867	2.650	31.93	0.287		0.012
1.883	2.656	31.86	0.277		0.012
1.900	2.662	31.79	0.305		0.012
1.917	2.668	31.73	0.278		0.012
1.933	2.674	31.66	0.296		0.012
1.950	2.680	31.60	0.287		0.012
1.966	2.685	31.53	0.290		0.012
1.983	2.691	31.47	0.289		0.012
2.000	2.697	31.40	0.299		0.013

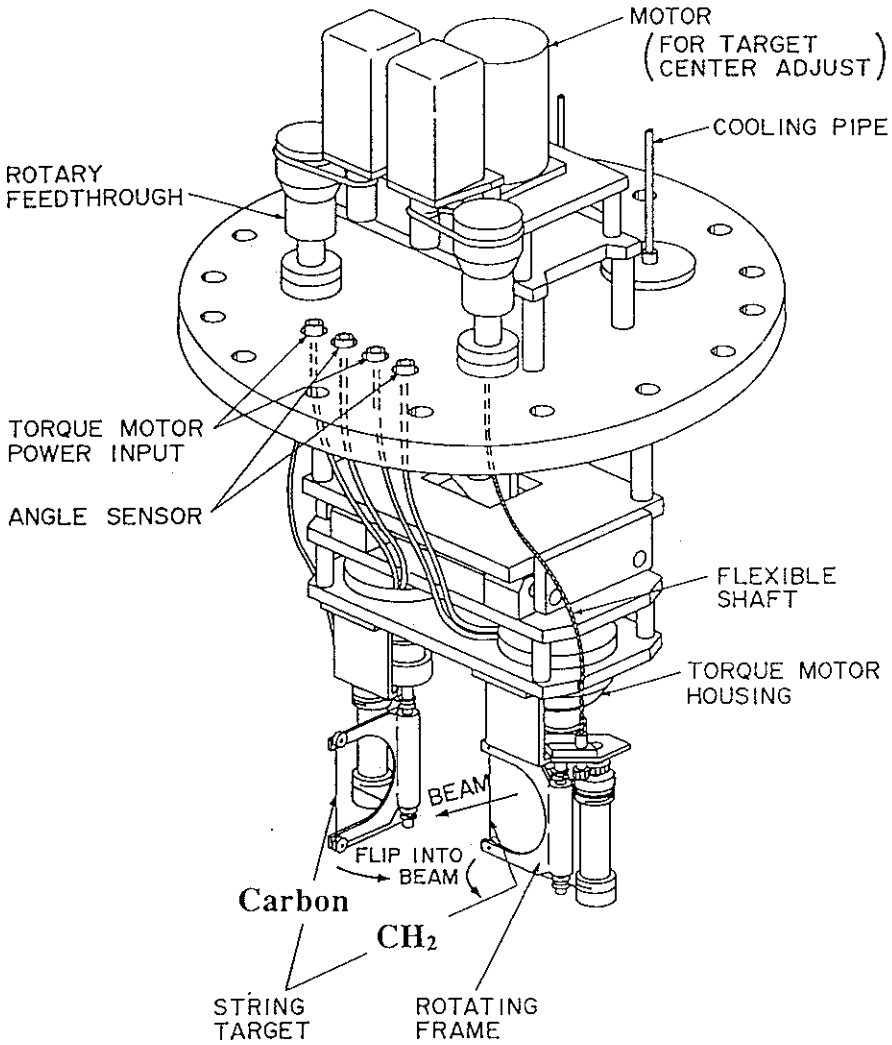

Fig.1

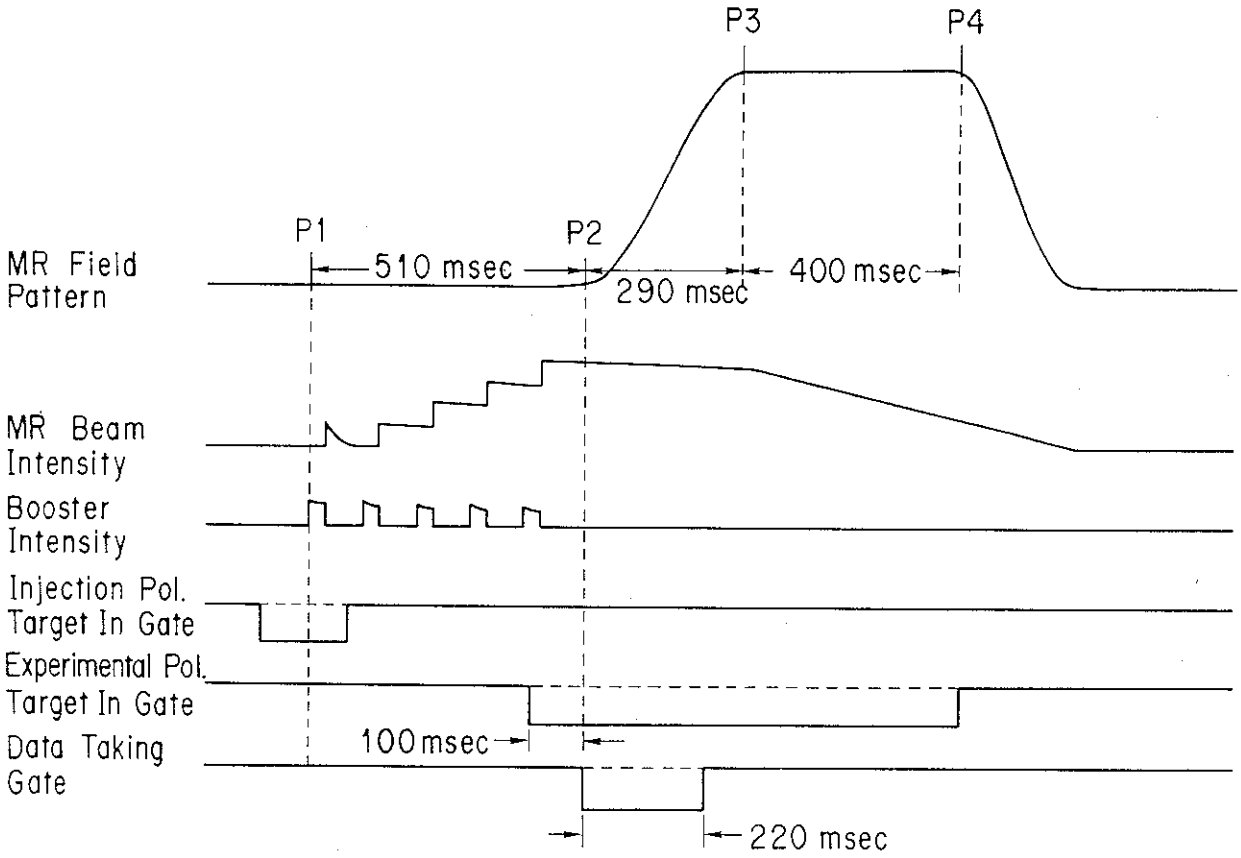
P3
P4
P1
P2
MR Field Pattern
510 msec
290 msec
400 msec
MR Beam Intensity
Booster Intensity
Injection Pol. Target In Gate
Experimental Pol. Target In Gate
Data Taking Gate
100 msec
220 msec

Fig.3

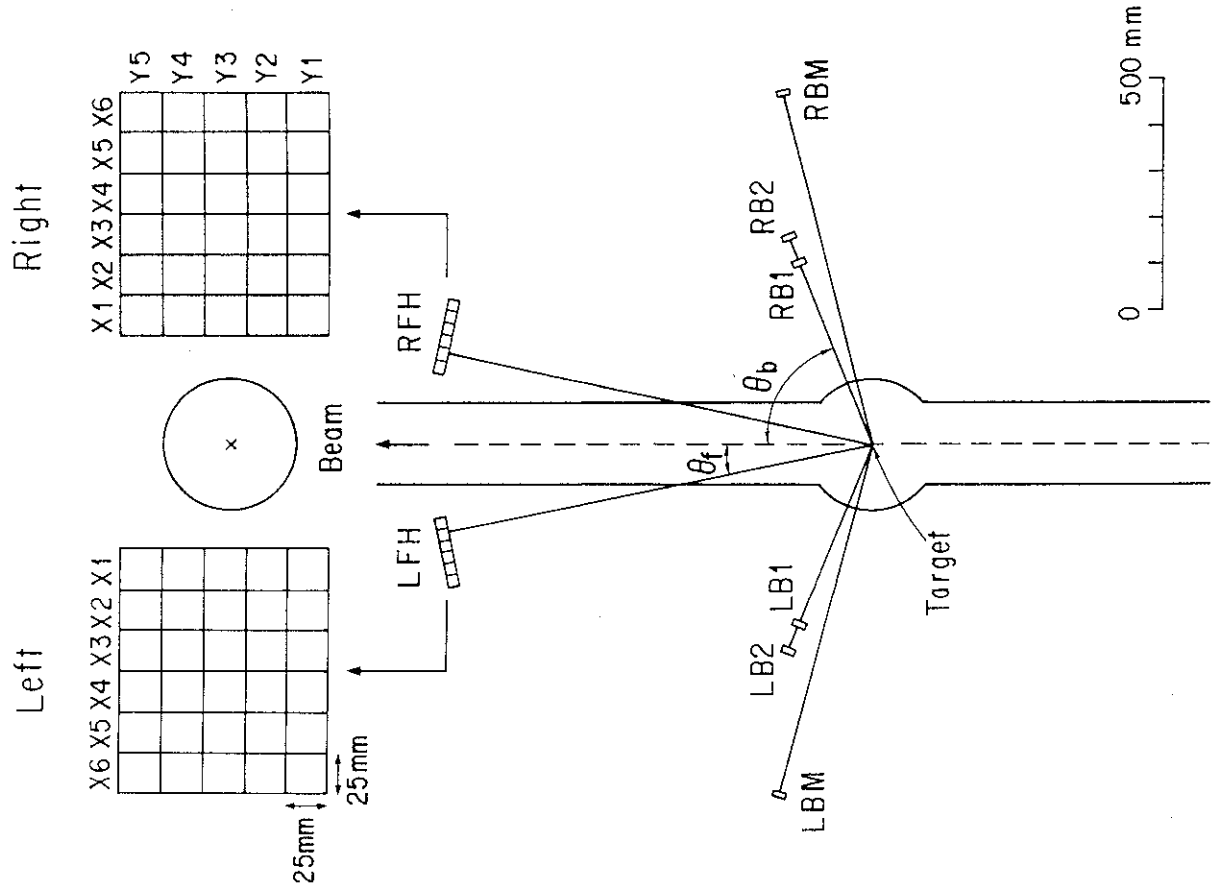
Right
Y5 Y4 Y3 Y2 Y1
X1 X2 X3 X4 X5 X6
RFH
Beam
LFH
Left
X6 X5 X4 X3 X2 X1
25mm
25mm
RBM
RB2
RB1
LB1
LB2
LBM
Target
500 mm
0

Fig.2

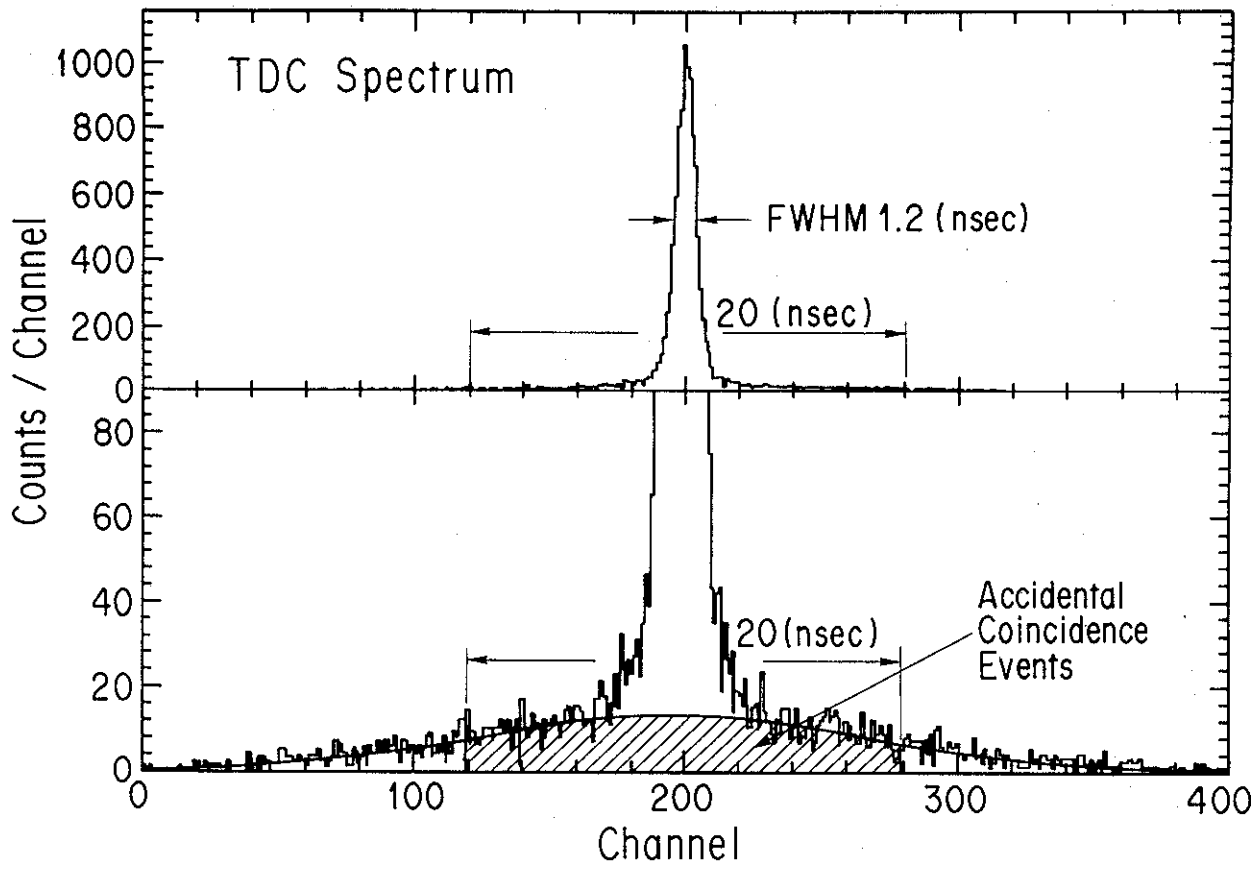
TDC Spectrum
Counts / Channel
FWHM 1.2 (nsec)
20 (nsec)
20 (nsec)
Accidental
Coincidence
Events
Channel
0
100
200
300
400
0
200
400
600
800
1000
0
20
40
60
80

Fig.5

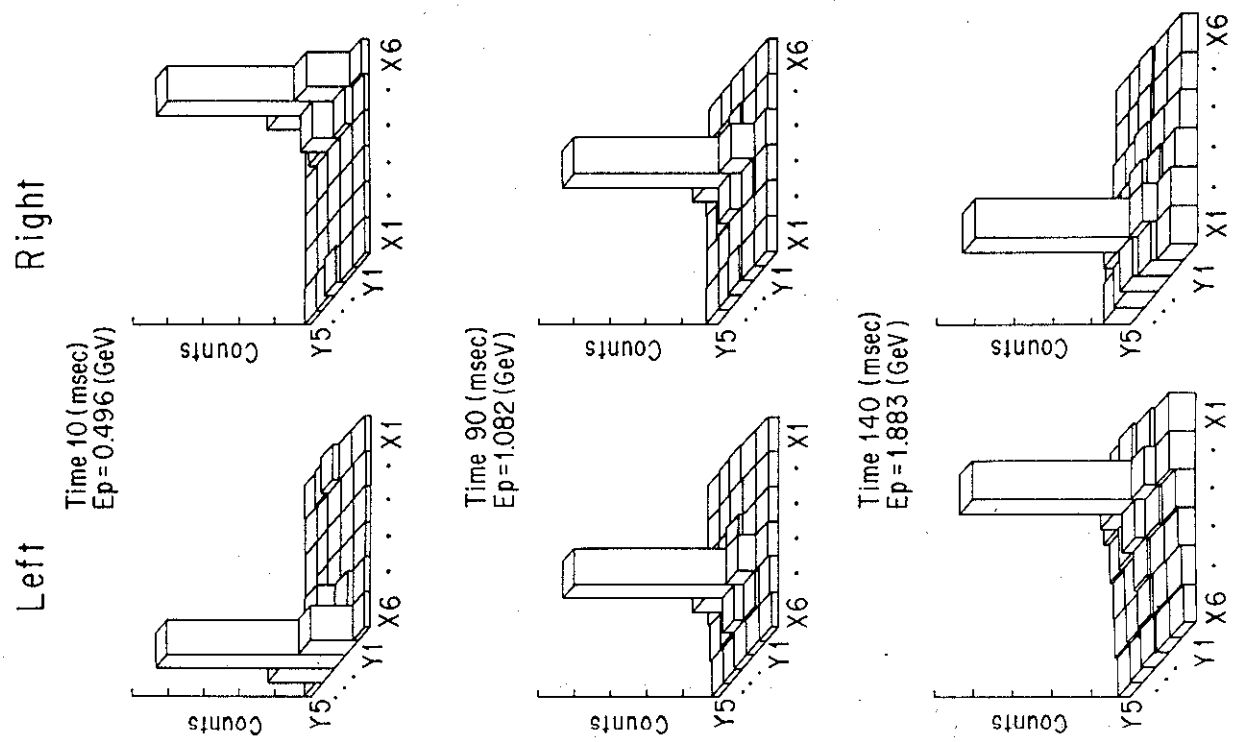
Right
Left
Time 10 (msec)
Ep=0.496 (GeV)
Time 90 (msec)
Ep=1.082 (GeV)
Time 140 (msec)
Ep=1.883 (GeV)
Counts
Y5
Y1
X1
X6

Fig.4

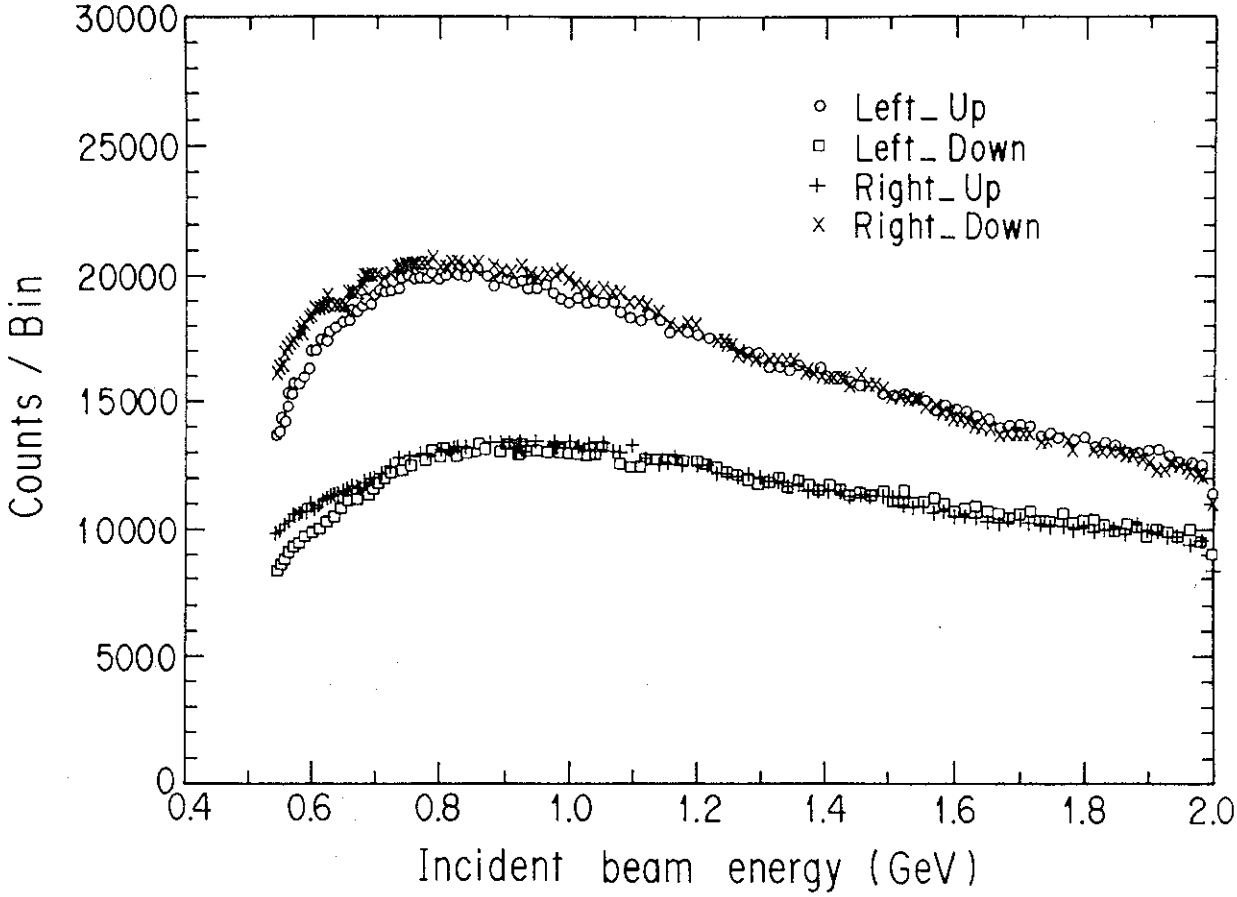
Left_Up
Left_Down
Right_Up
Right_Down
Counts / Bin
Incident beam energy (GeV)

Fig.7

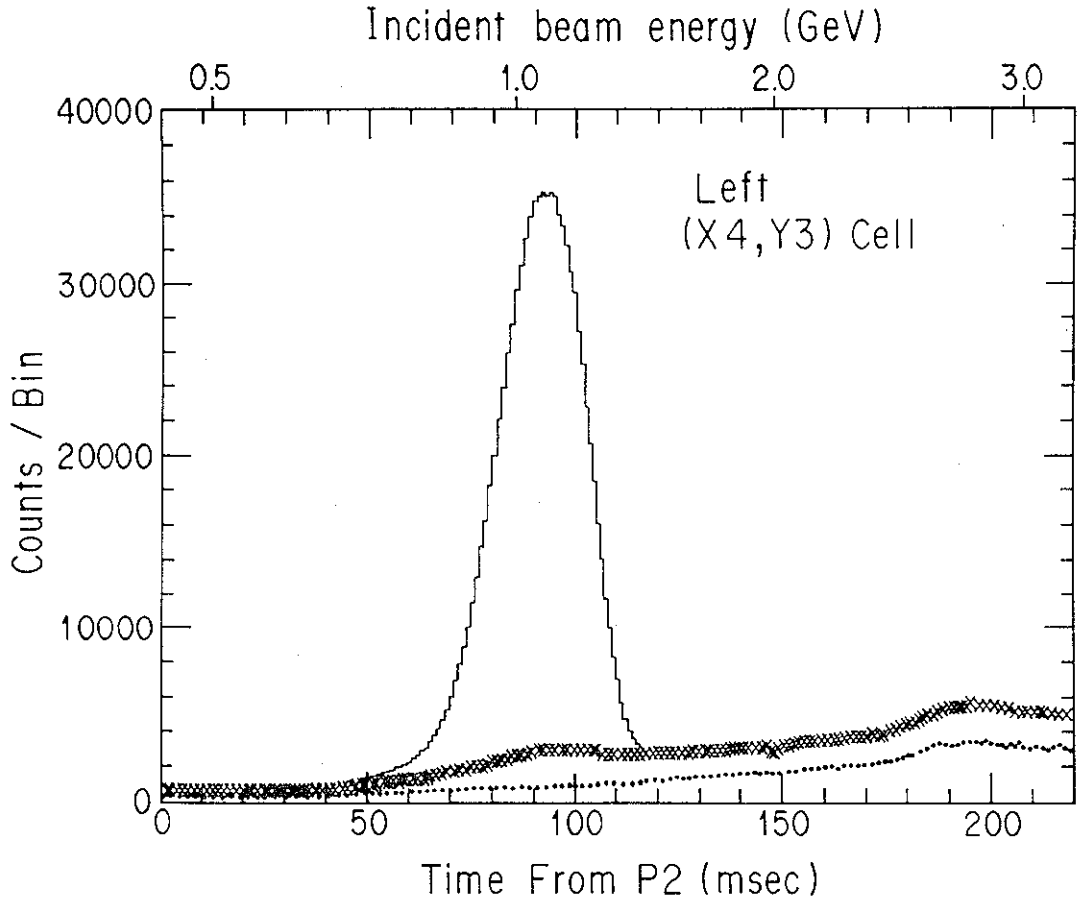
Incident beam energy (GeV)
Left
(X4,Y3) Cell
Counts / Bin
Time From P2 (msec)

Fig.6

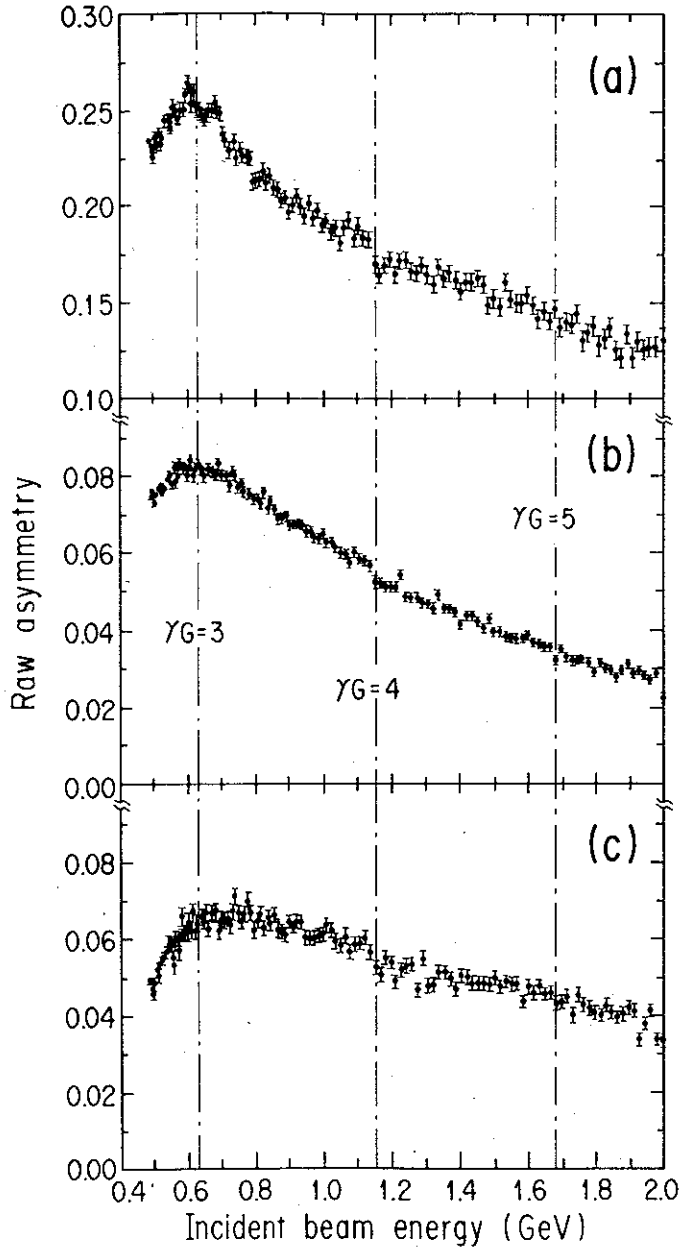
(a)
(b)
(c)
γG=3
γG=4
γG=5
Raw asymmetry
Incident beam energy (GeV)

Fig.8

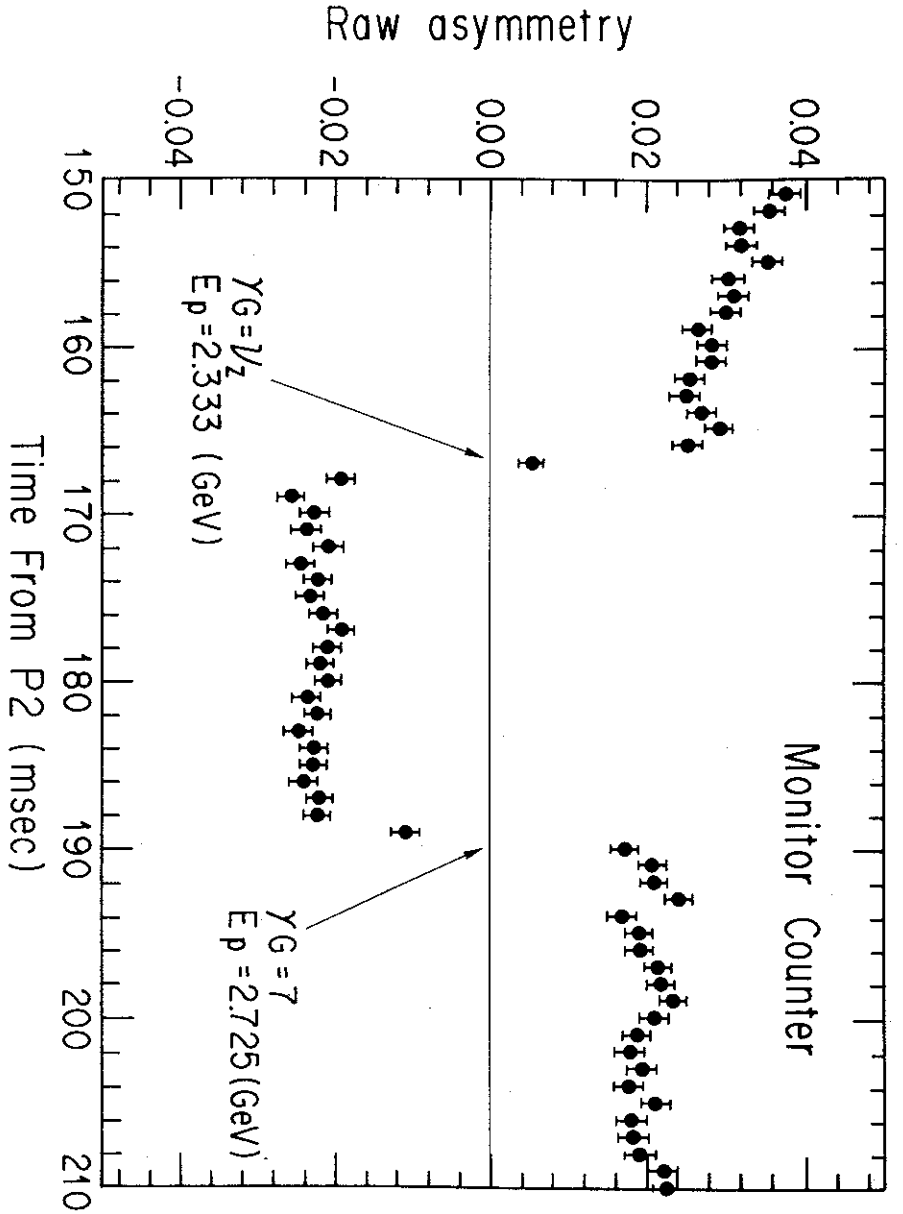
Raw asymmetry
Time From P2 (msec)
Monitor Counter
γG=1/2
Ep=2.333 (GeV)
γG=7
Ep=2.725(GeV)

Fig.9

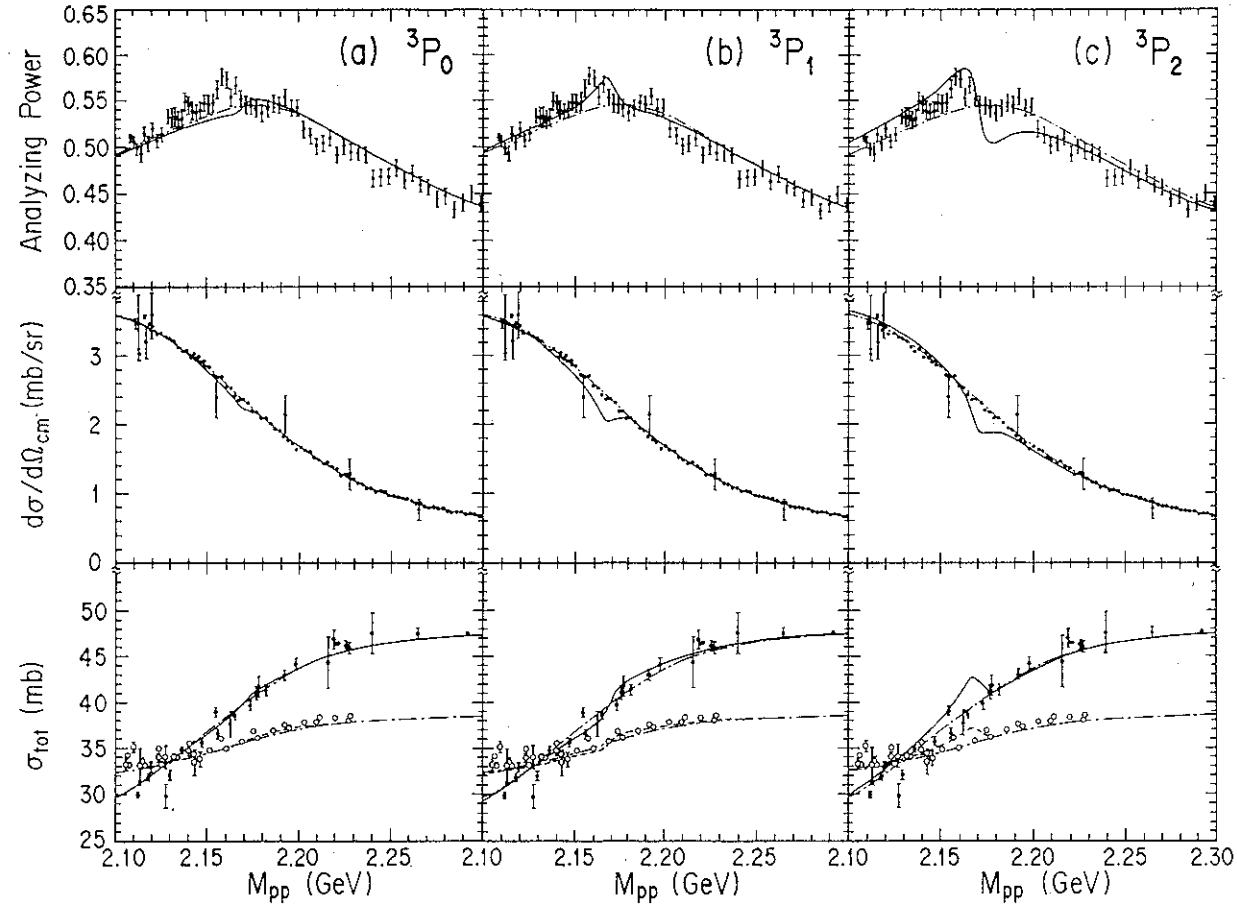
(a) $^3P_0$
(b) $^3P_1$
(c) $^3P_2$
Analyzing Power
$d\sigma/d\Omega_{cm.}$ (mb/sr)
σ_{tot} (mb)
M_{pp} (GeV)

Fig.11

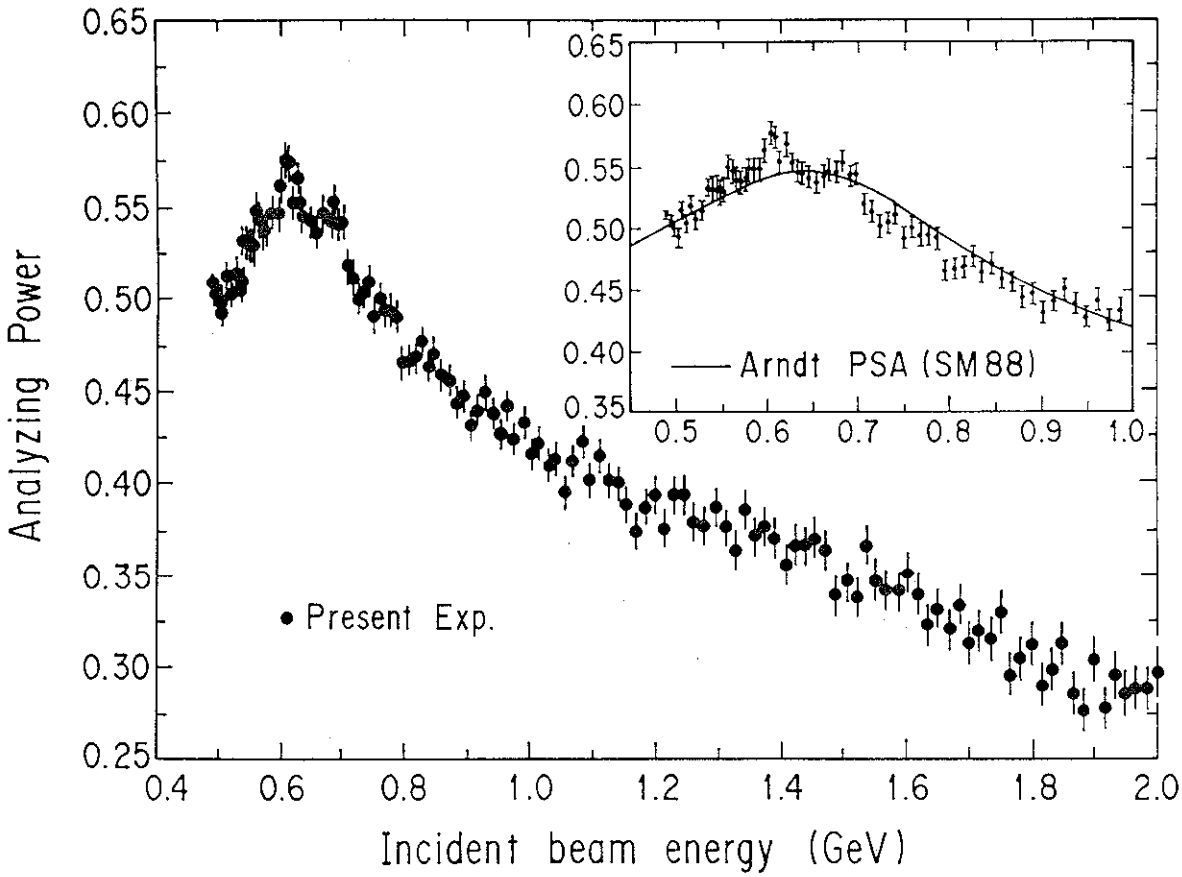
Analyzing Power
Incident beam energy (GeV)
• Present Exp.
—— Arndt PSA (SM88)

Fig.10

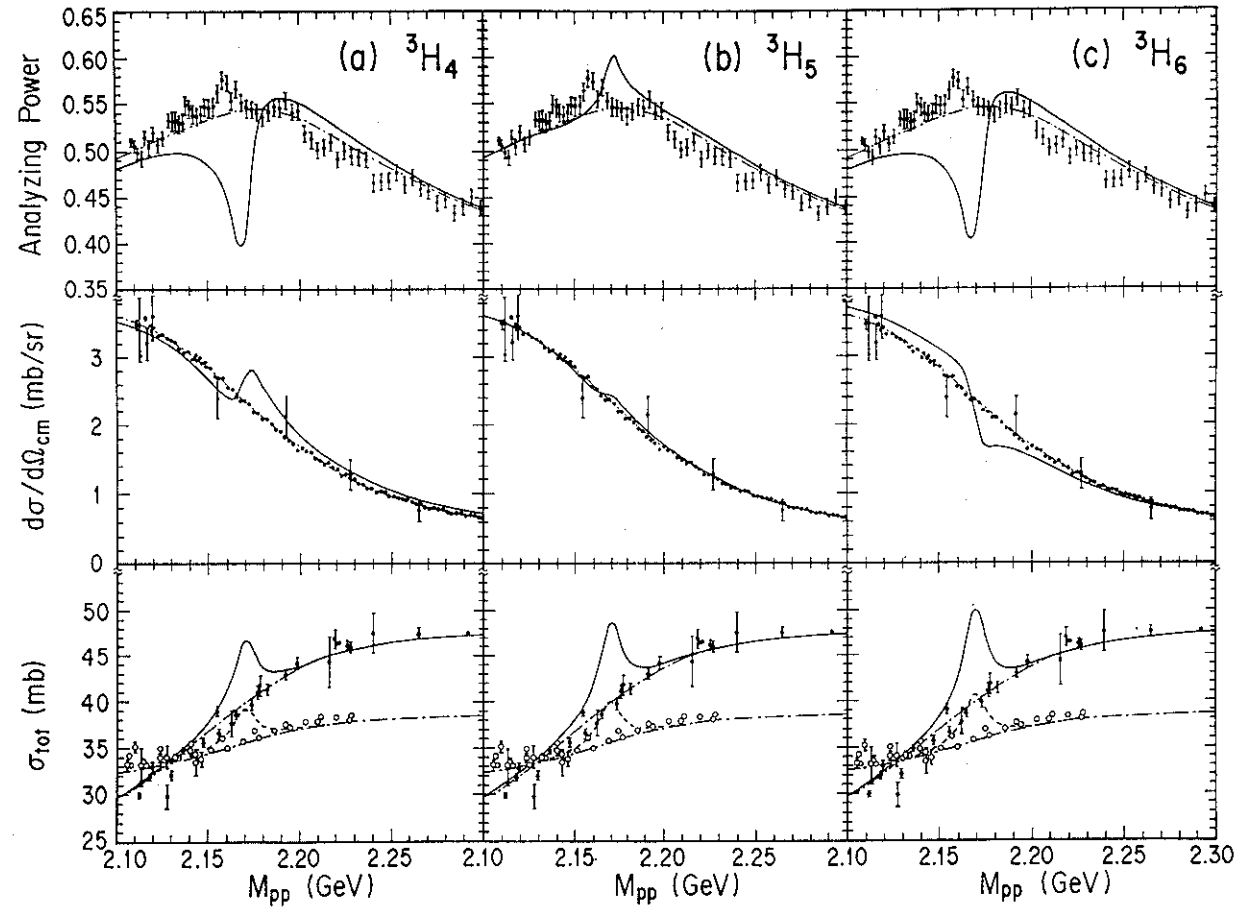
(a) $^3H_4$
(b) $^3H_5$
(c) $^3H_6$
Analyzing Power
$d\sigma/d\Omega_{cm}$ (mb/sr)
σ_{tot} (mb)
M_{pp} (GeV)

Fig.13

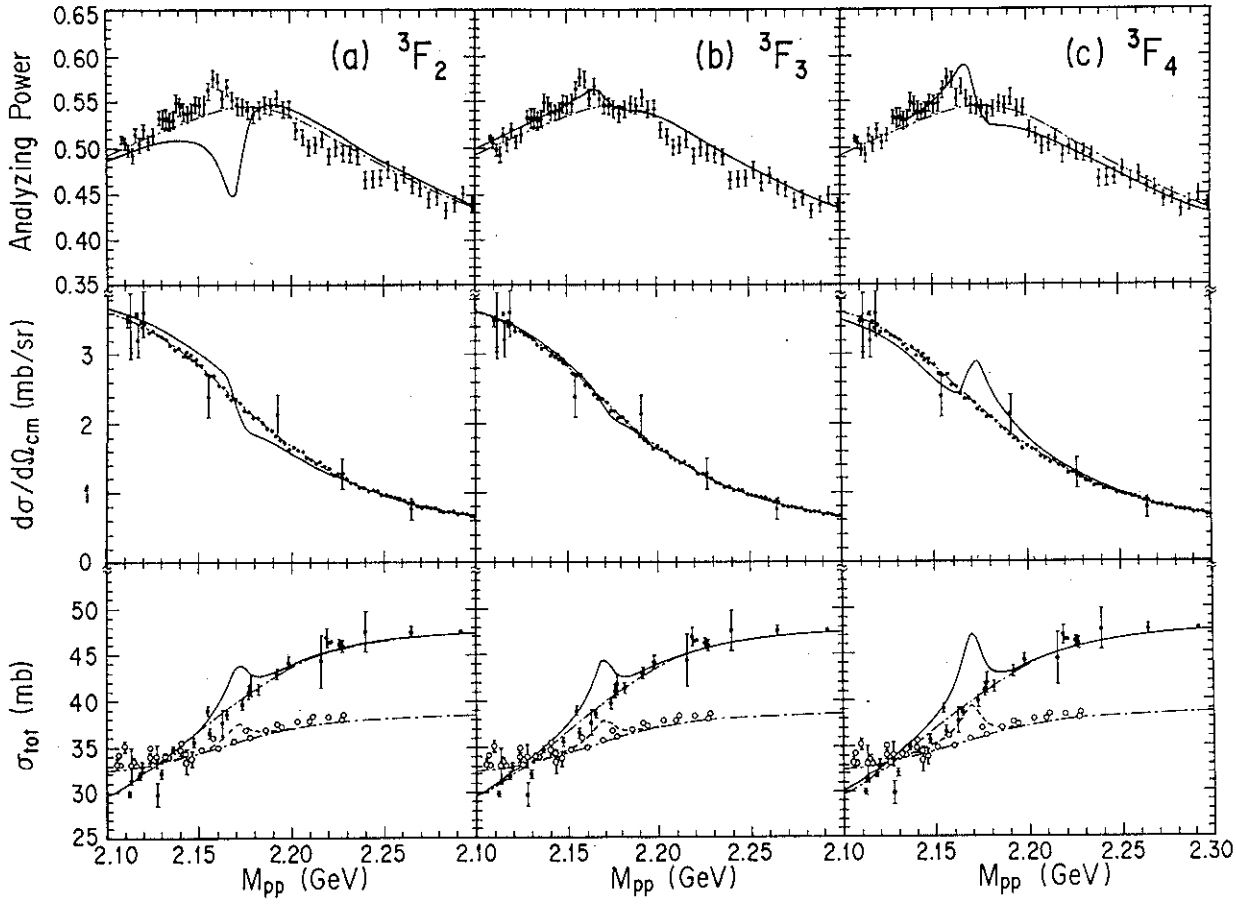
(a) $^3F_2$
(b) $^3F_3$
(c) $^3F_4$
Analyzing Power
$d\sigma/d\Omega_{cm}$ (mb/sr)
σ_{tot} (mb)
M_{pp} (GeV)

Fig.12

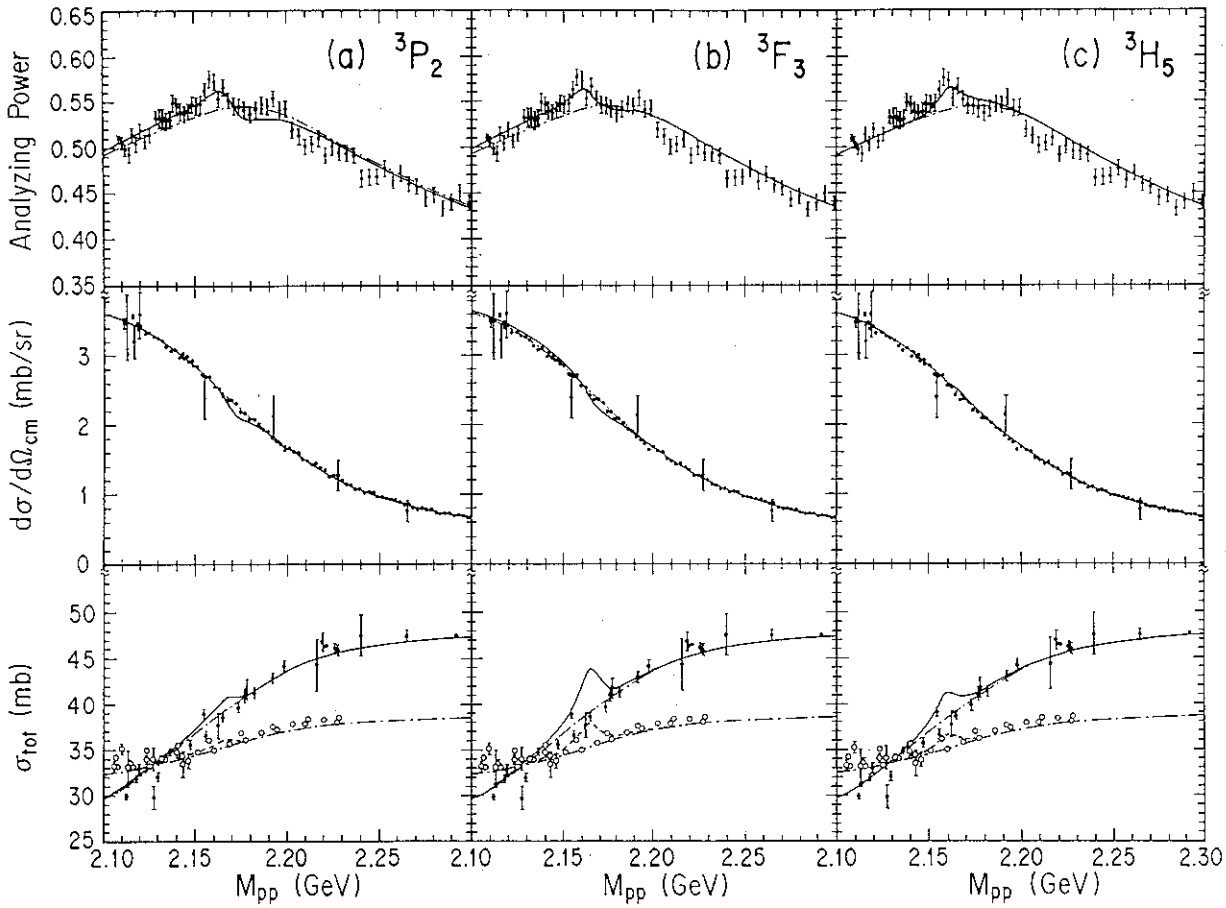
(a) $^3P_2$
(b) $^3F_3$
(c) $^3H_5$
Analyzing Power
$d\sigma/d\Omega_{cm}$ (mb/sr)
σ_{tot} (mb)
M_{pp} (GeV)

Fig.15

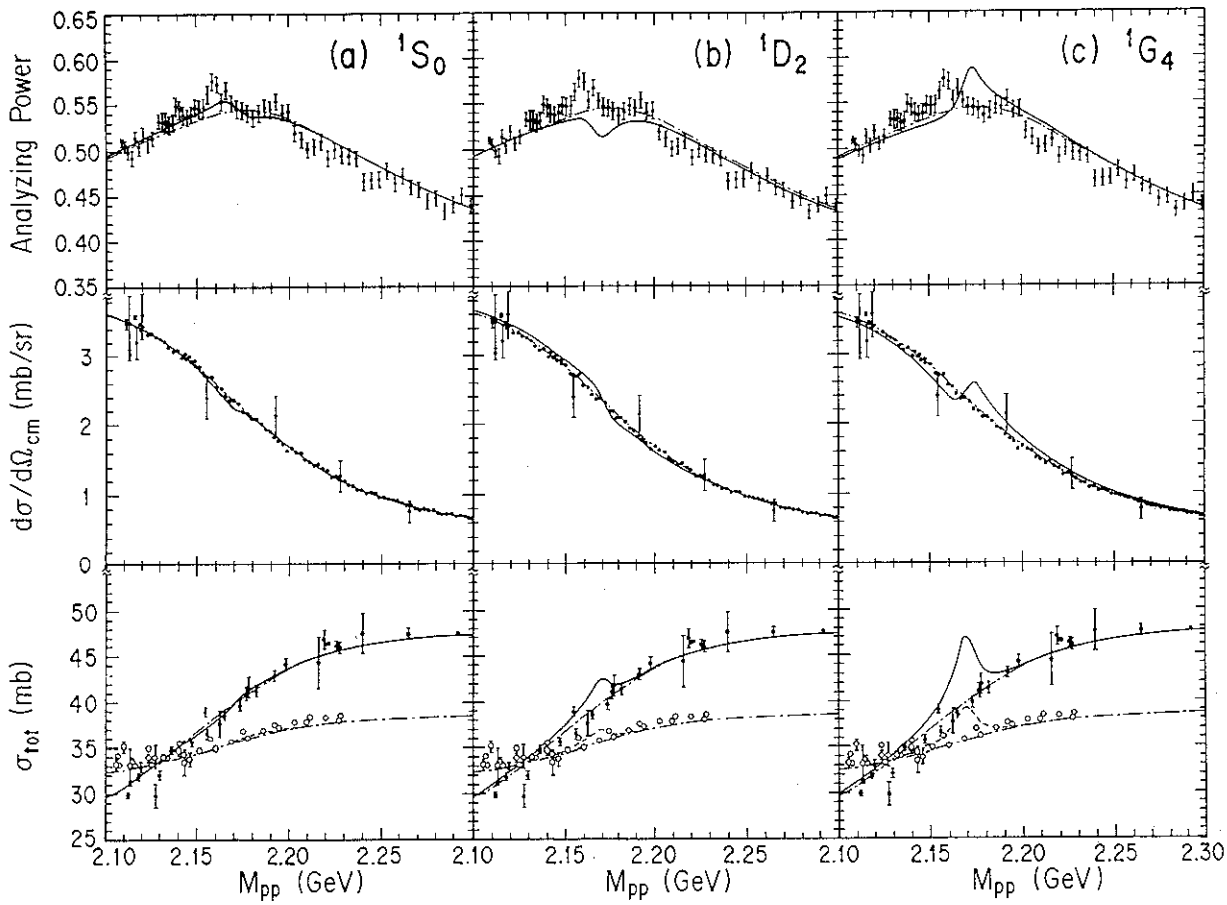
(a) $^1S_0$
(b) $^1D_2$
(c) $^1G_4$
Analyzing Power
$d\sigma/d\Omega_{cm}$ (mb/sr)
σ_{tot} (mb)
M_{pp} (GeV)

Fig.14